Article

Oxygen Evolution Reaction on the Fe$_3$O$_4$(001) Surface: Theoretical Insights into the Role of Terminal and Bridging Oxygen Atoms

Giulia Righi, Stefano Fabris, and Simone Piccinin*

Cite This: *J. Phys. Chem. C* 2021, 125, 18752−18761

Read Online

ACCESS | Metrics & More | Article Recommendations | SI Supporting Information

ABSTRACT: Model catalysts, where the structure of single-crystal materials with well-defined surface terminations can be determined at the atomic level, are useful systems to perform fundamental studies on electrocatalysis. The magnetite Fe$_3$O$_4$(001) surface, in particular, has been the focus of several studies aimed at characterizing its structure in vacuum in the presence of a water layer and interfaced with liquid water-based electrolytes. Recently, this system has also been investigated as a catalyst for the oxygen evolution reaction (OER), with the goal of correlating structural properties of the interface with catalytic performance and mechanism. In this work, we use first-principles simulations based on density functional theory to establish the structural, thermodynamic, and electronic properties of the Fe$_3$O$_4$(001) surface in contact with water. We compute the phase diagram of the magnetite/water system and address some open issues on the structural transitions observed experimentally among different surface terminations. We then address the stability in electrochemical environments, and we investigate the OER mechanism, considering reaction paths involving both terminal and bridging oxygen atoms. We find that different surface reconstructions can promote OER *via* different reaction sites and potential-determining steps, albeit with a similar energy cost. In particular, the bulk-truncated termination promotes OER *via* terminal oxygen atoms, and the potential-determining step is the dehydrogenation of the *OH group. On the ($\sqrt{2} \times \sqrt{2}$)R45° reconstruction, on the other hand, OER proceeds *via* the bridging oxygen atoms, and the potential-determining step is the formation of the hydroperoxo.
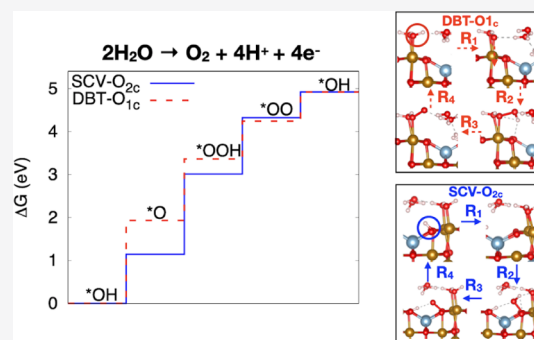
INTRODUCTION

Electrochemical water splitting is an emerging technology for the production of so-called green hydrogen,[1−3] generating increasing interest both as a means to store energy from excess renewable energy sources in the form of a high-energy-density fuel and as an alternative to the traditional production of hydrogen from fossil fuels. The process is composed of two half-reactions: the cathodic hydrogen evolution reaction and the anodic oxygen evolution reaction (OER). One of the key factors limiting the efficiency of the overall process is the sizeable energy loss caused by the high overpotentials of the OER,[4] which is usually considered to be the bottleneck of the electrochemical production of hydrogen.[5]

Among the various materials employed as electrocatalysts (and photoelectrocatalysts) for OER, transition-metal oxides represent an extremely versatile class, comprising compounds like IrO$_2$, the only material that is both highly active and stable in acidic environments,[6] and NiFe-oxyhydroxides, among the most efficient catalysts in alkaline environments.[7] In spite of tremendous advances in our understanding of the mechanism of OER,[5] it is still not clear how metal oxides promote this reaction, and the reaction mechanism appears to be strongly material-dependent. OER is usually assumed to proceed *via* a series of proton-coupled electron transfer (PCET) on surface

metal atoms, with the O−O bond formation taking place *via* nucleophylic attack of a water molecule (or a hydroxide ion in alkaline environments) on an oxo ligand.[8−10] This mechanism is sometimes referred to as the adsorbate evolution mechanism.[11] Some materials, however, can promote OER *via* the direct coupling of two oxo ligands, for example, Co-based electrocatalysts.[12,13] Moreover, recent experiments[14,15] have shown that some perovskites can promote OER *via* the lattice oxygen mechanism, involving the oxidation of oxygen atoms of the catalysts rather than the adsorbates; this mechanism is favorable when there are empty oxygen p-states above the redox energy of the O$_2$/H$_2$O couple.[15]

Often, the interpretation of the experimental findings is hampered by difficulty of characterizing the structure of the interface between the catalyst and the electrolyte. Experiments on model systems,[16] where the structure of single-crystal catalysts with well-defined surface terminations can be
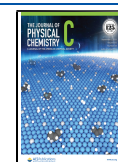
determined at the atomic level, can be an invaluable tool to further our understanding of the mechanism of OER. A number of reports by Parkinson and co-workers on magnetite (Fe_3O_4) go precisely in this direction.[17−21] The $Fe_3O_4(001)$ surface orientation in particular, besides being the lowest energy surface, is also the most investigated and best understood of the low-index facets of magnetite.[18] Measurements performed in ultra-high vacuum (UHV) established that the surface exposes a $(\sqrt{2} \times \sqrt{2})R45°$ reconstruction.[18,22] Several surface models have been proposed to explain this reconstruction. Of particular interest are the distorted bulk truncated (DBT) model[22] and the subsurface cation vacancy (SCV) model.[17] The latter has been shown to agree well with the experimental low-energy electron diffraction (LEED) pattern and to be energetically the most stable under UHV conditions and is therefore the accepted model to explain the reconstruction.[17]

Several surface science experiments and theoretical investigations have been dedicated to understand how water molecules adsorb on the $Fe_3O_4(001)$ surface in UHV in the low coverage limit. Recently, Meier et al.,[20] using a combination of quantitative temperature-programmed desorption, high-resolution X-ray photoelectron spectroscopy (XPS), and density functional theory (DFT) calculations, have found that a single water molecule adsorbs molecularly on the most stable surface reconstruction. When water dimers are present, the most stable adsorption mode is a partially dissociated form, where one molecule is adsorbed molecularly and the second is dissociated. This mixed, partially dissociated adsorption mode stems from a cooperative effect between water molecules and the surface, where the H-bond and water−surface interactions are maximized by the dissociation of one of the two molecules.[20,23] Higher water coverages lead to the appearance of partially dissociated water trimers and to ring-like patterns of partially dissociated water molecules.

Of particular interest is the experimental evidence that upon increasing the coverage of the adsorbed water molecules, the $(\sqrt{2} \times \sqrt{2})R45°$ reconstruction is lifted, restoring a bulk-like (1×1) termination.[24,25] A similar effect has also been measured upon adsorption of atomic H.[25,26] A recent work by Kraushofer et al.[19] has addressed this topic using a variety of experimental techniques, including scanning tunneling microscopy (STM), LEED, and XPS. The authors found that upon exposing the SCV-reconstructed $Fe_3O_4(001)$ surface to liquid water and then evacuating to UHV, the system undergoes a significant transformation, restoring the bulk-like (1×1) surface periodicity and enhancing the fraction of Fe^{2+} cations. Moreover, STM revealed the formation of ordered chain-like protrusions, assigned to hydroxyl species bound to Fe surface atoms, generated by dissociated water molecules. These protrusions are aligned along the $[110]$ direction, the same direction of the Fe rows in the SCV reconstruction, and straddle two Fe rows in the $[\bar{1}10]$ direction. The coverage of hydroxyl species is estimated to be around 2 per unit cell. A very similar effect was obtained upon exposure to 20 mbar water vapor at room temperature prior to evacuation to UHV.

In a recent theoretical work, Liu and Di Valentin[27] proposed a model for the $Fe_3O_4(001)$ surface exposed to water consisting of a four-water-molecule layer, partially dissociated and adsorbed on the bulk-like DBT termination. They predicted that under water-rich conditions, the DBT termination is more stable than the SCV reconstruction,

which would explain the experimental evidence. As pointed out by Kraushofer et al.,[19] however, the calculated phase transition occurs at oxygen and water chemical potentials which are not accessible at room temperature and UHV pressures.

Interestingly, electrochemical STM (EC-STM) performed in 0.1 M $NaClO_4$ (pH 7) also revealed chain-like features oriented along the $[110]$ direction, suggesting that the surface structure obtained upon water exposure and evacuation to UHV is representative of the solid−electrolyte interface at pH 7.[19] In an alkaline environment, on the other hand, the SCV surface reconstruction is maintained. Müllner et al.[28] have found that the SCV surface prepared in UHV is stable after exposure to an electrolyte in a pH range between 7 and 14. Moreover, the surface remains unchanged under OER conditions, probed by cyclic voltammetry.

The stability of the SCV surface in an electrochemical environment was confirmed recently by Grumelli et al.[21] The authors have found using in situ surface X-ray diffraction that after the immersion of the SCV surface in 0.1 M NaOH, the reconstruction was observed from −0.2 V versus Ag/AgCl to more positive values, whereas it disappears at more negative values of applied potential. The lifting of the surface proceeds gradually while lowering the potential. The system was then tested as a catalyst for OER. The experiments of Grumelli et al. suggest that the OER proceeds with the same mechanism on both the (001) surfaces since the current increases with the same Tafel slope, but the SCV is slightly more active. The applied potentials necessary to achieve a current density of 1 mA/cm^2 are 0.70 and 0.75 V versus Ag/AgCl in 0.1 M NaOH for the SCV and DBT surfaces, respectively, that is, the overpotentials at this current density are around 0.44 and 0.49 V, respectively.

This brief summary of some of the most interesting findings on the $Fe_3O_4(001)$/water interface shows that this is an ideal system to investigate how the structure of the interface relates to it OER properties since this is one of the few systems where such a detailed structural characterization has been achieved. In spite of this, there are a number of questions still open both in terms of structural properties of the interface and in terms of the actual mechanism of OER, where theoretical modeling can provide valuable insights.

In this work, using DFT calculations, we have investigated water adsorption on the $Fe_3O_4(001)$ surface and the mechanism of OER promoted by this system. First, we address the interaction between water and various $Fe_3O_4(001)$ terminations, considering novel structures compared to the existing literature and focusing in particular on the experimental observation concerning the lifting of the SCV surface reconstruction following the exposure to water. We then model OER considering both terminal and bridging oxygen atoms as possible reaction intermediates on both the DBT and SCV surfaces. We find that different surface terminations promote OER via different oxygen adsorbates and that in spite of this, the theoretical overpotential is very similar on the two surfaces, in good agreement with experiments.

■ COMPUTATIONAL METHODS

In our DFT calculations, performed using the Quantum ESPRESSO code,[29,30] we employed optimized norm-conserving Vanderbilt pseudopotentials to describe the interaction between ions and electrons.[31,32] We have used the Perdew, Burke, and Ernzerhof[33] approximation for the exchange and

correlation functional. The energy cutoff was set to 60 Ry, and the convergence criterion for the forces was set to 0.02 eV/Å. To describe the correlated Fe d electrons, we used the Hubbard correction as implemented by Cococcioni and de Gironcoli,[34] and the U value was determined using the linear response approach ($U = 4.1$ eV). Surfaces were modeled in (2 × 2) surface unit cells, and the Brillouin zone was sampled using a $3 \times 3 \times 1$ Monkhorst-Pack[35] grid of k-points. To avoid interactions between periodic replicas of the slabs, we inserted 15 Å of vacuum. During structural optimizations, the central layers of the slab were kept fixed to their bulk positions. To account for van der Waals interactions, we use Grimme's DFT-D3 approach.[36] To evaluate the electronic charge in individual atoms, we used both the Lödwin projection[37] and the Bader approach through the algorithm of Henkelman et al.[38] To account for the effects of the bulk solvent in electrochemical simulations, we used the implicit solvent model provided by the Environ code[39] coupled with Quantum ESPRESSO using the default parameters for the water solvent.

We have calculated the adsorption energy of water as

$$E_{ads} = \frac{1}{N_{H_2O}}(E_{total} - E_{Fe_3O_4} - N_{H_2O}E_{H_2O}) \quad (1)$$

where E_{total} is the total energy of the slab with N_{H_2O} adsorbed water molecules, $E_{Fe_3O_4}$ is the total energy of the pristine surface, and E_{H_2O} is the total energy of the water molecule, and water molecules have been adsorbed on both the top and bottom surfaces.

To determine the thermodynamic stability of various surface structures as a function of temperature and partial pressures, we computed the surface free energy of formation γ as a function of the oxygen and water chemical potentials as

$$\gamma(T, p_{O_2}, p_{H_2O}) = \frac{1}{2A}\left[E_{total} - \frac{1}{3}N_{Fe}E_{Fe_3O_4}\right.$$
$$+ \left(\frac{4}{3}N_{Fe} - N_O\right)\mu_O(T, p_{O_2})$$
$$- N_{H_2O}\mu_{H_2O}(T, p_{H_2O})$$
$$\left. - N_H\mu_H(T, p_{O_2}, p_{H_2O})\right] \quad (2)$$

where A is the area of the surface; E_{total} is the total energy of the full system including slab water adsorbates; $E_{Fe_3O_4}$ is the total energy of the bulk per formula unit; and μ_O, μ_H, and μ_{H_2O} are the oxygen, hydrogen, and water chemical potentials which depend on temperature T and partial pressures, respectively. The chemical potentials are related via $\mu_{H_2O} = 2\mu_H + \mu_O$. N_{Fe} and N_O are the numbers of iron and oxygen atoms, respectively. N_{H_2O} is the number of water molecules adsorbed on the surface. In eq 2, the Gibbs free energy of solids has been approximated with the total energy, thereby neglecting entropic effects. Temperature and pressure enter in eq 2 only through the chemical potential of the gas-phase reservoirs. The dependence of these chemical potentials on pressure is assumed to obey the ideal gas law

$$\mu_O(T, p_{O_2}) = \frac{1}{2}\left[\mu_{O_2}(T, p^0) + k_BT \ln\left(\frac{p_{O_2}}{p^0}\right)\right] \quad (3)$$

$$\mu_{H_2O}(T, p_{H_2O}) = \mu_{H_2O}(T, p^0) + k_BT \ln\left(\frac{p_{H_2O}}{p^0}\right) \quad (4)$$

where the temperature dependence of the chemical potentials at standard pressure $\mu(T, p^0)$ has been extracted from JANAF thermochemical tables.[40] In the following, we will refer the chemical potentials to their zero-temperature values, that is, the total energies of oxygen and water molecules, and we will therefore report the dependence of γ on $\Delta\mu_{O_2}$ and $\Delta\mu_{H_2O}$. The total energies of the oxygen and water molecules have been calculated in a box with a 20 Å edge. We have added zero-point energy (ZPE) corrections to the total energy of oxygen and water molecules as well as to water adsorbates using values obtained from the literature.[41]

To go beyond one of the main approximations employed in eq 2, namely, equating the free energies of solids with their total energies, one could consider the vibrational entropy of adsorbates, derived from normal mode analysis.[42] Campbell and Sellers,[43] however, have shown that this approximation may underestimate the entropic contribution of the adsorbates and that adsorbed molecules can retain around 2/3 of their gas-phase entropy. This is consistent with the fact that water molecules cannot be imaged with room-temperature STM due to their high mobility.[19] To account for this, we have modified eq 2 by adding an entropic contribution to non-dissociated water molecules equal to 2/3 of the gas-phase value. Here, we have compared both these approaches to describe the entropic contribution.

To simulate the STM images at applied bias V, we have used the Tersoff−Hamann model[44] as implemented in the Quantum ESPRESSO code, where the simulated images consist in a map of the local density of states integrated between the Fermi energy E_F and the energy $E_F - eV$.

■ RESULTS AND DISCUSSION

Interaction between Water Molecules and Magnetite Surfaces. Magnetite crystallizes in an inverse spinel structure with space group $Fd\bar{3}m$. All the tetrahedral iron atoms are in the oxidation state Fe^{3+}, whereas the octahedral irons can be in either the Fe^{3+} or Fe^{2+} oxidation state. We have studied both the DBT[22] and the SCV[17] magnetite surface reconstructions as shown in Figure 1. The SCV reconstruction is characterized by the introduction of a tetrahedral Fe atom in the sub-layer surface and by the removal of two octahedral Fe atoms in the third layer below the outermost layer, see Figure 1d. These surfaces were modeled using symmetric slabs composed of 17 layers. Inspired by experimental observations related to the lifting of the SCV surface reconstruction in humid environments, we have considered a surface reconstruction detected by Doudin et al.[45] during an ab initio molecular dynamics simulation with a surface coverage of 0.5 ML of hydrogen atoms. This surface reconstruction is characterized by a shift of the interstitial tetrahedral iron atom, which is a distinctive feature of the SCV reconstruction, to the third layer below the surface to refill one of the two Fe vacancies of the SCV, as shown in Figure 1g. We labeled this as surface SCV-mod. This new surface reconstruction goes in the direction of the bulk-truncated one since it loses the main characteristic of the SCV reconstruction, namely, the interstitial tetrahedral Fe atom.

To investigate the interaction between water and the Fe_3O_4 surface, we have first tested the adsorption of a single water molecule on the different surface reconstructions. In agreement
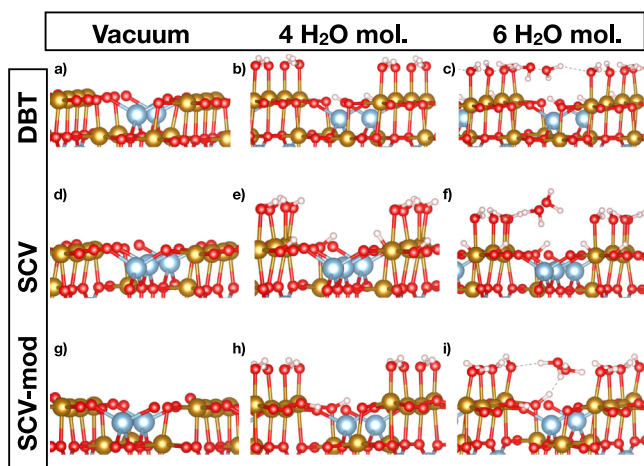
Figure 1. Side view of the (a) bulk truncated surface (DBT), (b) DBT with four water adsorbed molecules, (c) DBT with six water adsorbed molecules, (d) SCV surface, (e) SCV with four water adsorbed molecules, (f) SCV with six water adsorbed molecules, (g) modified subsurface cation vacancy (SCV-mod), (h) SCV-mod with four water adsorbed molecules, and (i) SCV-mod with six water adsorbed molecules. The yellow and light-blue balls are the octahedral and tetrahedral iron atoms, respectively. The red balls represent the oxygen atoms. The small white balls are the hydrogen atoms.

with previous reports,[20,27] we find that water adsorbs dissociatively on the DBT surface, with an adsorption energy of -0.85 eV, molecularly on the SCV surface, with an adsorption energy of -0.51 eV. SCV-mod behaves similar to the DBT termination, favoring dissociative adsorption, with an adsorption energy of -0.89 eV (see the Supporting Information).

When increasing the water coverage, we found that four water molecules prefer to adsorb in a mixed mode on both the DBT and SCV surfaces, as shown in Figure 1. A water molecule is adsorbed above each of the four surface octahedral Fe^{3+} atoms, and two of them are dissociated. One of the two hydrogen atoms of the water molecule forms a hydrogen bond with the closest OH group with an O–H distance of 1.45 Å.

Our results for the DBT and SCV surfaces are in agreement with previous theoretical works,[20,27] and the adsorption energies are reported in Table 1. The mixed mode of

Table 1. Adsorption Energies per Molecule (eV) on the DBT, SCV, and SCV-mod Surfaces[a]

N_{mol}	DBT	SCV	SCV-mod
4	−0.94 (−1.11)	−0.58 (−0.75)	−0.95 (−1.12)
6	−0.81 (−1.01)	−0.56 (−0.75)	−0.84 (−1.01)

[a]The values in parentheses have been obtained with the van der Waals correction. N_{mol} is the number of water molecules adsorbed on the surface.

adsorption is also favored on the SCV-mod surface. The adsorption energies are -0.58, -0.94, and -0.95 eV for the SCV, DBT, and SCV-mod surfaces, respectively. These adsorption energies per molecule are slightly more negative than those calculated for a single water molecule, see Table S1, particularly for the DBT and SCV-mod surfaces. This is due to a cooperative effect between surface bonding and hydrogen bonding active in agglomerates of partially dissociated water molecules, as discussed by Schiros et al.[23] and Meier et al.[20]

To simulate higher water coverages, we have adsorbed six molecules per unit cell on the surfaces. The extra two molecules have been adsorbed above the tetrahedral Fe atoms of the second layer below the outermost layer, and they move to form a new ring-like surface pattern, driven by the formation of H-bonds as shown in Figure 1. The obtained pattern is consistent with the STM measurements for the SCV surface by Meier et al.[20] and is similar to the one proposed by the same authors. We define as full coverage (1 ML) this configuration with six water molecules per unit cell, corresponding to one water molecule per Fe ion, considering both surface octahedral and subsurface tetrahedral Fe atoms.

In the experiments by Kraushofer et al.,[19] when the sample is re-evacuated following exposure to water, the authors observed the desorption of water, while some OH groups remained bound to the surface. The authors estimated a coverage of two hydroxyl groups per unit cell. This estimation is in agreement with the number of OH groups present on our water-covered surfaces.

The average adsorption energy per molecule is weaker than the one calculated with only four molecules adsorbed, particularly for the DBT and SCV-mod surfaces. This is because the extra two water molecules are now adsorbed on the tetrahedral Fe atoms, which are less favorable adsorption sites.

Surface Phase Diagram. To gain further insights into the thermodynamics of water adsorption on $Fe_3O_4(001)$, we have computed the surface free energy of formation as a function of the oxygen and water chemical potentials using eq 2. Due to the well-known overbinding of the oxygen molecule in GGA functionals, we have corrected the O_2 total energy in order to reproduce either the experimental formation energy of water or the experimental binding energy of O_2. In Figure 2, we show the phase diagrams obtained with the inclusion of the van der Waals correction, the entropic correction for adsorbed water molecules obtained from normal mode analysis, and the total energy of the oxygen molecule corrected to reproduce the binding energy of the oxygen molecule. In the Supporting Information, Figure S5, we report phase diagrams obtained with different corrections.

Under water-poor conditions (corresponding to a low water partial pressure), the clean SCV surface is the most stable reconstruction in a wide range of oxygen chemical potentials. The phase transition from the SCV surface to the DBT surface occurs at $\Delta\mu_O = -2.21$ eV when reproducing the binding energy of the oxygen molecule and at -1.50 eV when the total energy of the oxygen molecule is corrected to reproduce the experimental formation energy of water as shown in Figure S5b. Experiments by Bliem et al.[17] showed that the SCV structure is more favorable at 10^{-8} mbar at 900 K, corresponding to $\Delta\mu_O = -1.98$ eV, which suggests that to obtain the results in agreement with these measurements, we need to employ a correction for the total energy of oxygen based on the binding energy of O_2. We note that the transition from SCV to DBT in the theoretical calculations of Bliem et al.[17] and Liu and Di Valentin[27] takes place at even lower values of $\Delta\mu_O$ ($\simeq -3.1$ and -2.6 eV, respectively). The SCV-mod surface, on the other hand, is never stable under water-poor conditions.

Next, we investigate water-rich conditions. Besides all the structures introduced so far, we also considered the possibility of excess H atoms residing at the surface, originating from the evolution of oxygen from water. These structures, indicated
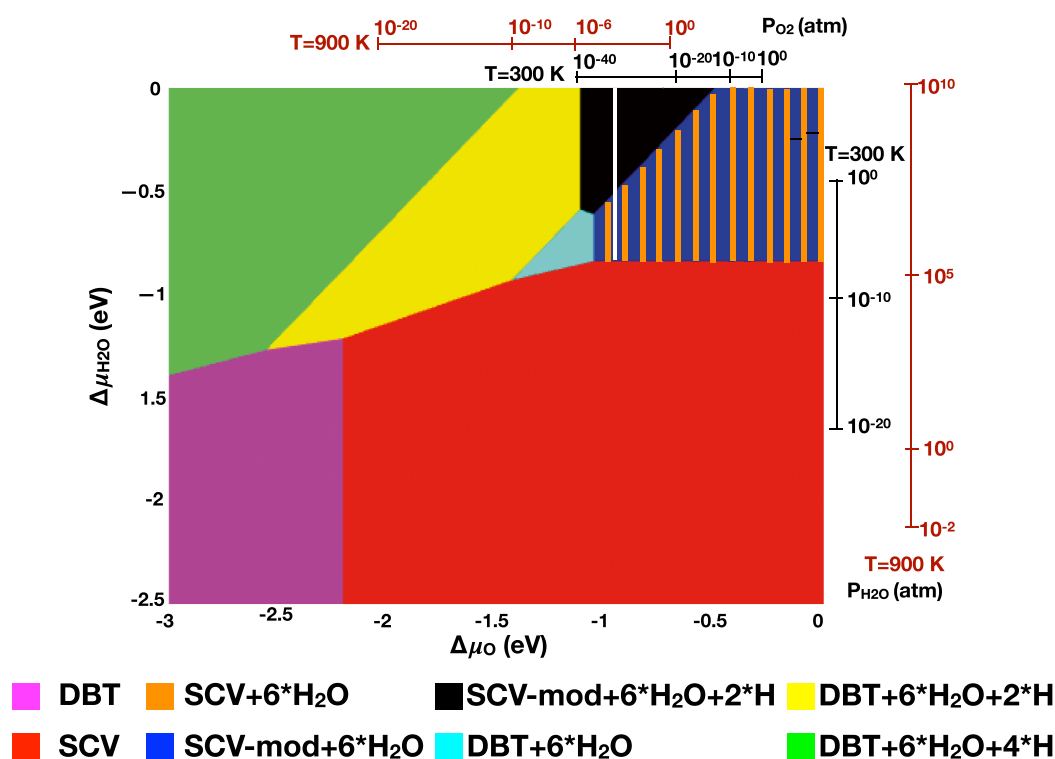
Figure 2. Magnetite phase diagrams as a function of oxygen ($\Delta\mu_O$) and water chemical potential ($\Delta\mu_{H_2O}$). The white line indicates the transition between water-covered DBT and SCV (SCV-mod) surfaces with four water molecules. We use this transition to compare our results with the experiment of Kraushofer et al.[19]

with the label *H in Figure 2, become increasingly more favorable as the chemical potential of water increases and the chemical potential of oxygen decreases. The atomic structures of these systems are reported in the Supporting Information (Figure S6). Notice that without the inclusion of the entropic corrections, the water-covered DBT surface with six water molecules is never stable.

In particular, we find that at low values of $\Delta\mu_O$, the most favorable surface is the DBT termination, covered with six water molecules per unit cell (1 ML coverage) and with adsorbed hydrogen. Increasing the oxygen chemical potential, we find that the most stable surfaces are the water-covered SCV and SCV-mod surfaces [the dashed area in Figure 2 indicates that the surface free energy of these two structures is nearly degenerate since they differ by just 50 meV per (2×2) cell]. Notice that among all the water coverages we considered, only those corresponding to six water molecules per unit cell appear in the phase diagram. The surfaces with different water coverages have indeed higher surface formation free energies, and consequently, they are less stable.

As shown in Figure 2, the transition from SCV to water-covered SCV and SCV-mod takes place at $\Delta\mu_{H_2O} = -0.84$ eV, while it occurs at a significantly lower water chemical potential ($\Delta\mu_{H_2O} = -1.41$ eV) if we estimate the entropic contribution as proposed by Campbell and Seller, as shown in Figure S5a. We note that without the entropic correction, the transition takes place at -0.76 eV, as shown in Figure S5c. Experimentally, Kendelewicz et al.[46] have observed the dissociative adsorption mode, at room temperature, only above 10^{-5} mbar. Under these conditions, the water chemical potential is -0.77 eV. Thus, the entropic contribution evaluated on the basis of the analysis of normal modes yields
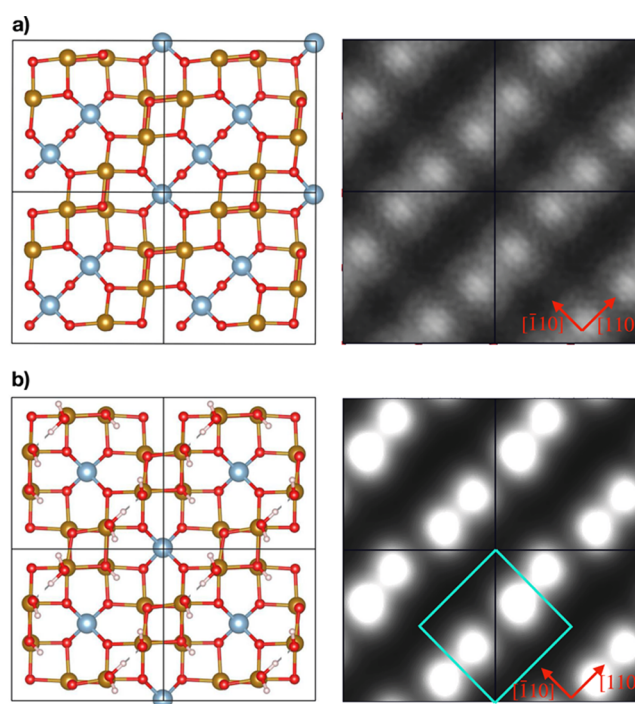

Figure 3. (a) Top view of the SCV surface and the corresponding STM image and (b) top view of the DBT with four water molecules adsorbed in a mixed mode and the corresponding STM image. The sample was held at a bias of 1.08 V. The cyan box indicates the (1×1) unit cell.

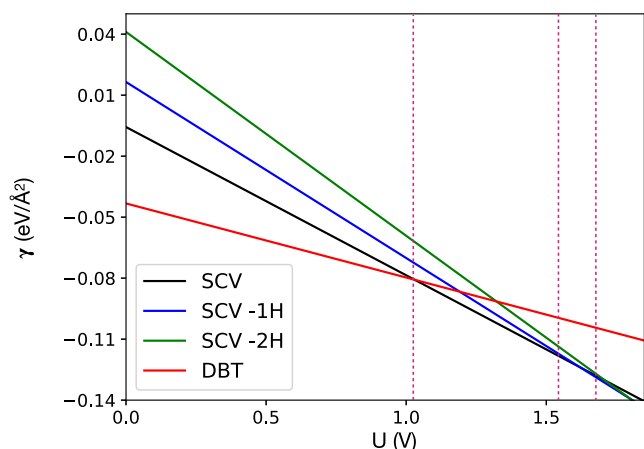a prediction of the phase transition to water-covered surfaces in good agreement with experiments, whereas the approx-

Figure 4. Surface free energy γ as a function of the applied bias U measured on the RHE scale.

imation proposed by Campbell and Seller[43] appears to overestimate the entropic stabilization of the water adsorbates.

Considering now the transition between the SCV (or equivalently SCV-mod) and DBT water-covered surfaces, this takes place at $\Delta\mu_O = -1.03$ eV when correcting the total energy of O_2 with its experimental binding energy and at $\Delta\mu_O = -0.51$ eV when reproducing the experimental formation energy of water (see Figure S5b).

In the experiment of Kraushofer et al.,[19] the SCV surface is exposed to water vapor at 20 mbar for 5 min and then evacuated to UHV at room temperature for analysis. Following this treatment, the $(\sqrt{2} \times \sqrt{2})R45°$ reconstruction is lifted, and a bulk-like (1×1) periodicity is restored. In UHV, the molecularly adsorbed water molecules desorb, and consequently, only the dimers, which are strongly bonded to the surface, might remain adsorbed. Therefore, to compare the calculated phase diagram with this specific experiment, we have considered only the four molecules adsorbed in a mixed mode. The transition between water-covered SCV and DBT (with only four molecules adsorbed), indicated by the white line in Figure 2, takes place around $\Delta\mu_O = -0.95$ eV. At room temperature, this would correspond to a pressure that is too low to be accessible in UHV chambers. We notice that Liu and Di Valentin estimated a similar, although slightly lower, value of $\Delta\mu_O$ for this transition.[27] An alternative explanation could be that the transition revealed by LEED measurements is not between the water-covered SCV and DBT surfaces but rather between SCV and SCV-mod surfaces, which our calculations indicate having nearly degenerate surface energies. The latter, in fact, has a (1×1) periodicity of the Fe ions, similar to the DBT termination.

In the same experiment, Kraushofer et al.[19] revealed by XPS measurements that after water exposure, the fraction of Fe^{2+} increases with respect to the $(\sqrt{2} \times \sqrt{2})R45°$ SCV surface which is Fe^{3+}-enriched. This finding would be consistent with a transition to the DBT surface, while it is not consistent with a transition to the SCV-mod surface since this retains the stoichiometry of the SCV. We note, however, that the reduction of Fe^{3+} to Fe^{2+} could also have other origins, for example, the dissolution of the material, as revealed by the emergence of structural defects after water exposure.[19]

Simulated STM Images. Simulated STM images of the pristine and water-covered surfaces are shown in Figure 3. To simulate the STM image of the water-covered surface re-

evacuated to UHV, we have considered only the dimers adsorbed on the DBT surface as shown in Figure 3b. Before the exposure to water, we observe rows of bright protrusions along the [110] direction due to the surface Fe atoms, see Figure 3a, in agreement with the STM measurements by Kraushofer et al.[19] After the exposure to water (see Figure 3b), rows of protrusions along the [110] direction are still present, but they are brighter than on the pristine surface, and a (1×1) pattern is found as indicated in Figure 3b. The calculated (1×1) pattern is similar to the one observed by Kraushofer et al.[19] in the high-density coverage regions after the surface was exposed to water for a long time and then re-evacuated to vacuum. Since the outermost layer of the water-covered SCV and DBT surfaces is the same, STM measurements are unable to reveal a transition between these two structures.

Stability of the Magnetite Surface in an Electrochemical Environment. As discussed in the previous section, a change in the chemical potentials of the gas-phase reactants can result in phase transitions among various surface structures. Similarly, in an electrochemical environment, the electrochemical potentials of protons and electrons, as determined by the pH and the applied potential, can result in structural transformations. Experimentally, Grumelli et al.[21] reported a transition from the DBT surface to the SCV surface above −0.2 V versus Ag/Cl at pH = 13, which corresponds to 0.76 V on the RHE scale.

To make contact with this experimental evidence, we use the computational hydrogen electrode approach of Nørskov and co-workers.[41] In this approach, one exploits the equilibrium 1/2$H_2 \rightleftharpoons H^+ + e^-$ at $p(H_2)$ = 1 bar, T = 298 K, pH = 0 at $U(SHE)$ = 0, that is, the sum of the chemical potentials of protons and electrons at pH = 0 and at zero applied bias on the SHE scale is equal to the chemical potential of gas-phase hydrogen under standard conditions. A non-zero external bias modifies the chemical potential of the electrons by $-eU$, where e is the electronic charge, while a non-zero pH modifies the chemical potential of the protons by $-k_BT \times \ln(10) \times$ pH, where k_B is Boltzmann's constant. We include ZPE and entropic corrections (TS), as prescribed in the original work of Nørsvok et al.[41] The ZPEs have been obtained from the analysis of the normal modes of the water adsorbates on the magnetite surfaces, whereas the contributions for the molecules in the gas phase are taken from ref 41. The entropic contributions of the adsorbed species are very small and consequently neglected,[47] while they are included for gas-phase molecules. The values of ZPE and entropic corrections are reported in the Supporting Information.

Considering the oxide surfaces to be in equilibrium with water, which acts as a reservoir of oxygen, we can write

$$\mu_H = \frac{1}{2}\mu_{H_2} - eU - k_BT \times \ln(10) \times \text{pH} \qquad (5)$$

$$\mu_O = \mu_{H_2O} - \mu_{H_2} + 2eU + 2k_BT \times \ln(10) \times \text{pH} \qquad (6)$$

The surface free energy, see eq 2, is therefore pH- and bias-dependent through the chemical potentials of oxygen and hydrogen.

Here, we focus on the relative stability of the DBT and SCV surfaces. We model the solid/liquid interface using a layer of explicit water, adopting the structural models identified in the previous section and comprising six water molecules per unit cell and modeling the effects of the bulk electrolyte through an implicit solvent model.
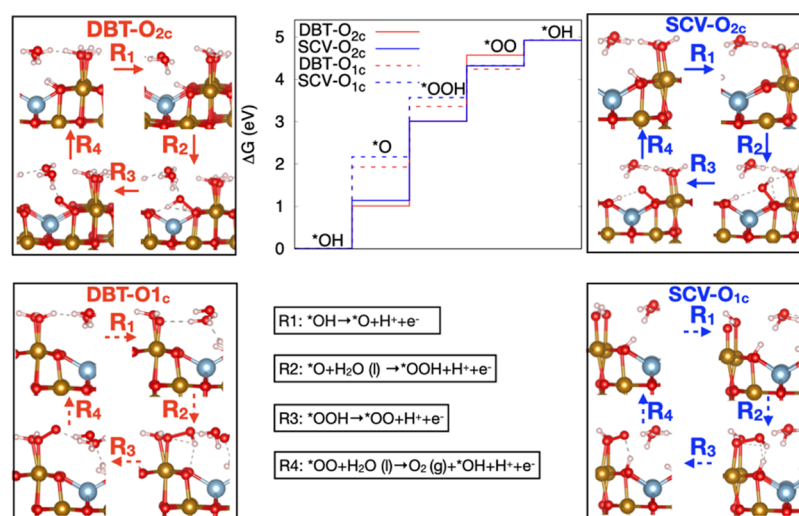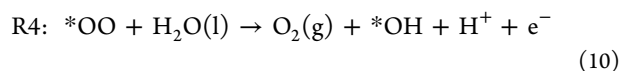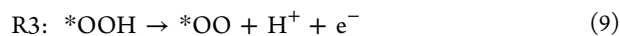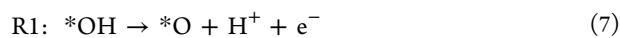
Figure 5. Reaction free-energy diagram of the OER reaction for the DBT and SCV surfaces, and a schematic picture of the OER on magnetite surfaces. The optimized intermediates for both the active sites are shown.

In Figure 4, we show the surface formation free energy of the DBT and SCV surfaces evaluated as a function of the applied bias, reported on the RHE scale. The unreconstructed DBT surface is stable below 1.02 V, while above this value, there is a transition to the SCV surface reconstruction. Notice that more oxidizing potentials favor the dehydrogenation of the SCV surface: we find that the removal of the first hydrogen atom takes place above 1.56 V (SCV-1H), while the removal of the second hydrogen atom happens above 1.69 V (SCV-2H). Our estimate of the transition (1.02 V on the SHE scale at pH = 0 or equivalently on the RHE scale) is therefore in fair agreement with the experimental measurement, with an error of 0.26 V.

OER on Magnetite Surfaces. Since Fe-oxides are promising candidates as low-cost catalysts for the OER in alkaline media, magnetite has been investigated experimentally through cyclic voltammetry to understand both its stability and catalytic activity toward OER.[21,28] We are not aware of previous theoretical investigations of catalytic properties of magnetite toward OER.

To model the OER, we considered the conventional sequence of PCET steps reported in eqs 7−10, where * indicates an empty site and *OH, *O, *OOH, and *OO represent the hydroxyl, oxo, hydroperoxo, and superoxo intermediates adsorbed on the empty site, respectively,

$$R1: \ *OH \rightarrow \ *O + H^+ + e^- \tag{7}$$

$$R2: \ *O + H_2O(l) \rightarrow \ *OOH + H^+ + e^- \tag{8}$$

$$R3: \ *OOH \rightarrow \ *OO + H^+ + e^- \tag{9}$$

$$R4: \ *OO + H_2O(l) \rightarrow O_2(g) + \ *OH + H^+ + e^- \tag{10}$$

In the first reaction step (R1), we have the first PCET step, the dehydrogenation of a hydroxyl group. R2 leads to the formation of the hydroperoxo through a nucleophilic attack of a water molecule on the oxo adsorbate. Reaction step R3 leads to the formation of a superoxo. In the last reaction step (R4), O_2 is released in solution, and water is adsorbed at the empty site as a hydroxyl group with a concomitant PCET. Reactions 7−10 are written in an acidic environment, but when reported on the RHE scale, the thermodynamics of the elementary steps

is identical regardless of whether acidic or alkaline environments are considered.[48] The free-energy cost (ΔG) of each of these steps has been evaluated using the computational hydrogen electrode.

We have investigated two possible active sites for OER: (i) a site involving terminal oxygen atoms, bound to an octahedral surface Fe cation (labeled as O_{1c}), and (ii) a site involving bridging oxygen atoms, coordinated with two surface octahedral Fe atoms (labeled as O_{2c}).

In Figure 5, we show the energy cost of the elementary steps performed on both the water-covered DBT and SCV surfaces, considering sites involving either terminal (O_{1c}) or bridging (O_{2c}) oxygen atoms, together with a schematic illustration of the structures corresponding to the various water oxidation intermediates.

In Table 2, we report the free-energy costs of the PCET steps for the four cases considered. We find that regardless of

Table 2. Free-Energy Cost (in eV) of the Four PCET Steps of the OER Reaction Considering a Singly Coordinated (Terminal) Oxygen Atom (O_{1c}) or a Doubly Coordinated (Bridge) Surface Oxygen (O_{2c}) as an Active Site for the DBT and SCV Surfaces

	DBT-O_{1c}	SCV-O_{1c}	DBT-O_{2c}	SCV-O_{2c}
ΔG_{R1}	1.93	2.17	1.01	1.14
ΔG_{R2}	1.43	1.40	2.00	1.88
ΔG_{R3}	0.88	0.75	1.56	1.31
ΔG_{R4}	0.68	0.60	0.35	0.59

the surface and site, the most demanding step is in all cases either R1 or R2. In the following, we therefore analyze in detail these two steps.

We begin our analysis by considering the mechanism involving the terminal oxygen O_{1c}. On both the DBT and SCV surfaces, the free-energy cost of the first PCET is the most demanding step of the overall reaction. The dehydrogenation of the *OH group (R1) results in a remarkable decrease of the magnetic moment of the surface Fe bound to the OH group, an indication of the oxidation of the cation from Fe^{3+} to Fe^{4+}. In spite of similar local environments and variations of Fe magnetic moments, the R1 step is more demanding (by 0.24

eV) on the SCV surface compared to the DBT surface. As discussed below, this is true also when R1 is performed on a bridging site (where the difference is 0.13 eV), suggesting that the dehydrogenation of *OH is in general more demanding on the SCV. To rationalize this result, we have computed the adsorption energy of the oxygen atom (E_{ads}^O) on the two surfaces since it has been established that the cost of the formation of the oxo intermediate scales approximately linearly with the adsorption energy of oxygen.[8] Defining $E_{ads}^O = 0$ eV through the equilibrium $H_2O \leftrightarrow$ *O $+H_2$, we found that for the SCV, $E_{ads}^O = -1.12$ eV, while for the DBT, $E_{ads}^O = -1.32$ eV. This shows that the oxygen atom is more strongly bound on the DBT surface, and we therefore expect the R1 step to be less demanding on this surface, in agreement with our findings. In the Supporting Information, we provide an analysis of the projected density of states (PDOS) of the two surface structures, showing that on the SCV surface, a localized peak in the middle of the gap appears due to the *O and Fe^{4+} atoms, whereas on the DBT surface, the same peak is closer to the top of the valence band.

The formation of the hydroperoxo intermediate (O−O bond length 1.46 Å) in step R2 leads to a reduction of the magnetic moment of the Fe atom to the value prior to the dehydrogenation, consistent with the expected reduction of the metal center to Fe^{3+}. On both surfaces, the hydroperoxo forms a hydrogen bond with a surface lattice oxygen.

Next, we consider the involvement of a bridging oxygen O_{2c}. Interestingly, different from the previous case, the free-energy cost of the first PCET is almost the same for both the surfaces. This is mirrored in almost identical geometries (O−Fe bond lengths of 2.08 and 2.13 Å in a bridge geometry in both cases). Moreover, the analysis of Bader charge and magnetic moments yields similar results on the two surfaces: step R1 leads to a decrease of the electronic charge (by about 0.5 e) of the oxygen atom, recovering the electronic charge of the unprotonated bridge surface oxygen atoms. Different from the previous case, also, the PDOS of both surfaces does not change appreciably upon performing the R1 step.

The free-energy cost of step R2, which leads to the formation of a hydroperoxo group, is slightly lower (by 0.12 eV) for the SCV surface. This difference can be understood by comparing the two different configurations: on the SCV, the *OOH group forms two hydrogen bonds (see Figure 5), one with the hydroxyl group and the other with the hydrogen atom adsorbed on the surface, whereas on the DBT surface, the hydroperoxo forms only a single hydrogen bond with the surface oxygen atom.

Comparing the different catalytic sites, we note that the cost of the first PCET is much larger for the terminal O_{1c} compared to the bridging O_{2c} (see Table 2). The opposite is true for the second step, the formation of the hydroperoxo. This is consistent with the fact that the sum of the costs of these two steps is roughly constant and independent of the material,[49] with the cost of R1 decreasing and the cost of R2 increasing as the oxo intermediate is bound more strongly. In our case, since the oxo intermediate is bound more strongly in the bridge geometry, this translates into R2 being the potential-determining step for this site, while R1 is the potential-determining step on the terminal site.

Comparing the DBT and SCV surfaces, our calculations indicate that OER on the unreconstructed DBT surface proceeds via the terminal oxygen O_{1c}, involving singly bound adsorbates on an unsaturated surface Fe site, and the most

demanding step is the dehydrogenation of the hydroxyl group (R1), leading to an estimated overpotential of 0.67 eV. On the SCV surface, on the other hand, OER takes place involving on a bridging oxygen O_{2c}, and the formation of the hydroperoxo is the potential-determining step, with an overpotential of 0.73 eV. Since both the potential-determining steps are PCET steps, it is unlikely that the two paths can be distinguished via an analysis of the Tafel slopes.[50] We also note that these values are similar to those calculated for Co_3O_4, an oxide with a spinel structure, by García-Mota et al.[4] and by Peng et al.,[51] considering a mechanism involving O_{1c}.

Comparing our findings with experimental measurements, our theoretical overpotentials are about 0.2 V larger than those obtained experimentally by Müllner et al.,[28] 0.48 V at 1 mA/cm^{-1}, and Grumelli et al.,[21] 0.44 and 0.49 V, on the SCV and DBT surfaces. Moreover, our calculations suggest that the DBT surface has a slightly lower (by 60 mV) overpotential compared to the SCV surface, while the opposite is true in measurements of Grumelli et al. (50 mV in favor of the SCV). Notice, however, that these differences are very small and certainly within the error bar of our methodology, considering both the intrinsic limitations imposed by the approximate exchange and correlation potential, the neglect of solvent effects, and the comparison of a thermodynamic quantity, the theoretical overpotential, with a kinetic parameter, the experimental overpotential.

Grimaud et al.[14,15] have shown that on some perovskite electrocatalysts, OER proceeds via the oxidation of surface lattice oxygen rather than oxygen atoms of water adsorbates. These surface lattice oxygen atoms are in fact bridging oxygen atoms, that is, they are structurally similar to the O_{2c} atoms considered here. A key finding of Grimaud et al. is that the involvement of lattice oxygen correlates with the presence of empty O(p) states below the redox potential of the O_2/H_2O couple.[15] As shown in the PDOS reported in the Supporting Information, however, this is not the case for our system: the Fermi level does not cut the O(p) band, which is completely filled. At least for magnetite, the involvement of lattice bridging oxygen atoms does not appear to require partially empty O(p) states.

Our findings on magnetite are in line with those of Carter and co-workers[52] on β-NiOOH, where different oxygen sites are found to be involved in OER, through different mechanisms but with very similar theoretical overpotentials. It is therefore possible that multiple oxygen active sites are involved on the same material either on the same facet as in magnetite or on different facets as in the case of β-NiOOH. Further experimental work on well-characterized surface terminations could help assessing the role of various surface oxygen atoms in OER.

■ CONCLUSIONS

In this work, we have explored the interaction of water molecules with the $Fe_3O_4(0001)$ surface, considering several surface structures and various coverages, ranging from a single molecule per unit cell to a full monolayer. When comparing with experiments, we found that our phase diagram can rationalize some of the measurements for this system, particularly the origin of protrusions seen in STM microscopy upon exposure to water, assigned to partially dissociated water adsorbates. We also found that the experimental evidence of the lifting of the $(\sqrt{2} \times \sqrt{2})R45°$ reconstruction and the

appearance the bulk-like (1×1) periodicity upon exposure to water could be due to the formation of the so-called SCV-mod structure, a termination with the same stoichiometry of the SCV reconstruction but with a bulk-like first layer of Fe ions.

We also modeled the system under eletrochemical conditions, addressing the relative stability of the SCV and DBT as a function of the applied bias. We found that an increasingly anodic bias drives the transition from the DBT structure to the SCV structure, in agreement with experiments.

We then performed the first theoretical study of the mechanism of OER on magnetite. We discovered that both terminal oxygen and bridging oxygen atoms can participate in the reaction and that the two surface structures considered, DBT and SCV, behave quite differently. The DBT promotes OER *via* the terminal oxygen, and the potential-determining step is the dehydrogenation of the *OH group. On the SCV surface, on the other hand, OER proceeds *via* the bridging oxygen, and the potential-determining step is the formation of the hydroperoxo. Comparing the predicted theoretical over-potentials, in spite of different potential-determining steps and different active sites, the two surfaces have similar thermodynamic requirements to make all elementary steps downhill in energy, with a slightly (60 mV) lower value for the DBT termination. The discovery that both terminal and bridging oxygen atoms can participate in OER with similar catalytic performances constitutes the main finding of our work.

ASSOCIATED CONTENT

Ⓢ Supporting Information

The Supporting Information is available free of charge at https://pubs.acs.org/doi/10.1021/acs.jpcc.1c05804.

Adsorption of a single water molecule, side view of a single water molecule adsorbed on the DBT, SCV, and SCV-mod surfaces, water adsorption energy per molecule, PDOS of various surface terminations changing the adsorption mode, variation of the Lödwin following the water adsorption, PDOS of the clean SCV-mod surface and with a single water molecule adsorbed on, PDOS of various surface terminations changing the coverage of water, ZPEs and entropic contributions for the adsorbed species and for molecules in the gas phase, modified surface free energy of formation γ with the entropic contribution, surface phase diagrams with various corrections, side view of the water-covered surfaces with two hydrogen atoms on surface oxygen atoms, and PDOS of the DBT and SCV surfaces without a hydrogen atom (PDF)

AUTHOR INFORMATION

Corresponding Author

Simone Piccinin − *Consiglio Nazionale delle Ricerche, Istituto Officina dei Materiali, CNR-IOM c/o SISSA, 34136 Trieste, Italy;* ⓞ orcid.org/0000-0002-3601-7141; Email: piccinin@iom.cnr.it

Authors

Giulia Righi − *Consiglio Nazionale delle Ricerche, Istituto Officina dei Materiali, CNR-IOM c/o SISSA, 34136 Trieste, Italy;* ⓞ orcid.org/0000-0003-4665-3691

Stefano Fabris − *Consiglio Nazionale delle Ricerche, Istituto Officina dei Materiali, CNR-IOM c/o SISSA, 34136 Trieste, Italy*

Complete contact information is available at:
https://pubs.acs.org/10.1021/acs.jpcc.1c05804

Notes

The authors declare no competing financial interest.

REFERENCES

(1) Shiva Kumar, S.; Himabindu, V. Hydrogen production by PEM water electrolysis − A review. *Mater. Sci. Technol.* **2019**, *2*, 442−454.

(2) Anantharaj, S.; Ede, S. R.; Sakthikumar, K.; Karthick, K.; Mishra, S.; Kundu, S. Recent Trends and Perspectives in Electrochemical Water Splitting with an Emphasis on Sulfide, Selenide, and Phosphide Catalysts of Fe, Co, and Ni: A Review. *ACS Catal.* **2016**, *6*, 8069− 8097.

(3) McHugh, P. J.; Stergiou, A. D.; Symes, M. D. Decoupled Electrochemical Water Splitting: From Fundamentals to Applications. *Adv. Energy Mater.* **2020**, *10*, 2002453.

(4) García-Mota, M.; Bajdich, M.; Viswanathan, V.; Vojvodic, A.; Bell, A. T.; Nørskov, J. K. Importance of Correlation in Determining Electrocatalytic Oxygen Evolution Activity on Cobalt Oxides. *J. Phys. Chem. C* **2012**, *116*, 21077−21082.

(5) Fabbri, E.; Schmidt, T. J. Oxygen Evolution Reaction: The Enigma in Water Electrolysis. *ACS Catal.* **2018**, *8*, 9765−9774.

(6) Nong, H. N.; et al. Key role of chemistry versus bias in electrocatalytic oxygen evolution. *Nature* **2020**, *587*, 408−413.

(7) Trotochaud, L.; Young, S. L.; Ranney, J. K.; Boettcher, S. W. Nickel−Iron Oxyhydroxide Oxygen-Evolution Electrocatalysts: The Role of Intentional and Incidental Iron Incorporation. *J. Am. Chem. Soc.* **2014**, *136*, 6744−6753.

(8) Rossmeisl, J.; Qu, Z.-W.; Zhu, H.; Kroes, G.-J.; Nørskov, J. K. Electrolysis of water on oxide surfaces. *J. Electroanal. Chem.* **2007**, *607*, 83−89.

(9) Dau, H.; Limberg, C.; Reier, T.; Risch, M.; Roggan, S.; Strasser, P. The Mechanism of Water Oxidation: From Electrolysis via Homogeneous to Biological Catalysis. *ChemCatChem* **2010**, *2*, 724− 761.

(10) Reier, T.; Nong, H. N.; Teschner, D.; Schlögl, R.; Strasser, P. Electrocatalytic Oxygen Evolution Reaction in Acidic Environments − Reaction Mechanisms and Catalysts. *Adv. Energy Mater.* **2017**, *7*, 1601275.

(11) Huang, Z.-F.; Song, J.; Du, Y.; Xi, S.; Dou, S.; Nsanzimana, J. M. V.; Wang, C.; Xu, Z. J.; Wang, X. Chemical and structural origin of lattice oxygen oxidation in Co−Zn oxyhydroxide oxygen evolution electrocatalysts. *Nat. Energy* **2019**, *4*, 329−338.

(12) Wang, L.-P.; Van Voorhis, T. Direct-Coupling O2 Bond Forming a Pathway in Cobalt Oxide Water Oxidation Catalysts. *J. Phys. Chem. Lett.* **2011**, *2*, 2200−2204.

(13) Mattioli, G.; Giannozzi, P.; Amore Bonapasta, A.; Guidoni, L. Reaction Pathways for Oxygen Evolution Promoted by Cobalt Catalyst. *J. Am. Chem. Soc.* **2013**, *135*, 15353−15363.

(14) Grimaud, A.; Hong, W. T.; Shao-Horn, Y.; Tarascon, J.-M. Anionic redox processes for electrochemical devices. *Nat. Mater.* **2016**, *15*, 121−126.

(15) Grimaud, A.; Diaz-Morales, O.; Han, B.; Hong, W. T.; Lee, Y.-L.; Giordano, L.; Stoerzinger, K. A.; Koper, M. T. M.; Shao-Horn, Y. Activating lattice oxygen redox reactions in metal oxides to catalyse oxygen evolution. *Nat. Chem.* **2017**, *9*, 457−465.

(16) Faisal, F.; et al. Electrifying model catalysts for understanding electrocatalytic reactions in liquid electrolytes. *Nat. Mater.* **2018**, *17*, 592−598.

(17) Bliem, R.; McDermott, E.; Ferstl, P.; Setvin, M.; Gamba, O.; Pavelec, J.; Schneider, M. A.; Schmid, M.; Diebold, U.; Blaha, P.; et al.

Subsurface cation vacancy stabilization of the magnetite (001) surface. *Science* **2014**, *346*, 1215−1218.

(18) Parkinson, G. S. Iron oxide surfaces. *Surf. Sci. Rep.* **2016**, *71*, 272−365.

(19) Kraushofer, F.; Mirabella, F.; Xu, J.; Pavelec, J.; Balajka, J.; Müllner, M.; Resch, N.; Jakub, Z.; Hulva, J.; Meier, M.; et al. Self-limited growth of an oxyhydroxide phase at the Fe3O4(001) surface in liquid and ambient pressure water. *J. Chem. Phys.* **2019**, *151*, 154702.

(20) Meier, M.; Hulva, J.; Jakub, Z.; Pavelec, J.; Setvin, M.; Bliem, R.; Schmid, M.; Diebold, U.; Franchini, C.; et al. Water agglomerates on Fe3O4(001). *Proc. Natl. Acad. Sci. U.S.A.* **2018**, *115*, E5642−E5650.

(21) Grumelli, D.; Wiegmann, T.; Barja, S.; Reikowski, F.; Maroun, F.; Allongue, P.; Balajka, J.; Parkinson, G. S.; Diebold, U.; Kern, K.; et al. Electrochemical Stability of the Reconstructed Fe3O4(001) Surface. *Angew. Chem., Int. Ed.* **2020**, *59*, 21904−21908.

(22) Pentcheva, R.; Wendler, F.; Meyerheim, H. L.; Moritz, W.; Jedrecy, N.; Scheffler, M. Jahn-Teller Stabilization of a "Polar" Metal Oxide Surface: Fe₃O₄(001). *Phys. Rev. Lett.* **2005**, *94*, 126101.

(23) Schiros, T.; Ogasawara, H.; Näslund, L.-Å.; Andersson, K. J.; Ren, J.; Meng, S.; Karlberg, G. S.; Odelius, M.; Nilsson, A.; Pettersson, L. G. M. Cooperativity in Surface Bonding and Hydrogen Bonding of Water and Hydroxyl at Metal Surfaces. *J. Phys. Chem. C* **2010**, *114*, 10240−10248.

(24) Mulakaluri, N.; Pentcheva, R.; Scheffler, M. Coverage-Dependent Adsorption Mode of Water on Fe3O4(001): Insights from First Principles Calculations. *J. Phys. Chem. C* **2010**, *114*, 11148−11156.

(25) Arndt, B.; Creutzburg, M.; Grånäs, E.; Volkov, S.; Krausert, K.; Vlad, A.; Noei, H.; Stierle, A. Water and Atomic Hydrogen Adsorption on Magnetite (001). *J. Phys. Chem. C* **2019**, *123*, 26662−26672.

(26) Parkinson, G. S.; Mulakaluri, N.; Losovyj, Y.; Jacobson, P.; Pentcheva, R.; Diebold, U. Semiconductor−half metal transition at the Fe₃O₄(001) surface upon hydrogen adsorption. *Phys. Rev. B: Condens. Matter Mater. Phys.* **2010**, *82*, 125413.

(27) Liu, H.; Di Valentin, C. Bulk-terminated or reconstructed Fe3O4(001) surface: water makes a difference. *Nanoscale* **2018**, *10*, 11021−11027.

(28) Müllner, M.; Riva, M.; Kraushofer, F.; Schmid, M.; Parkinson, G. S.; Mertens, S. F. L.; Diebold, U. Stability and Catalytic Performance of Reconstructed Fe3O4(001) and Fe3O4(110) Surfaces during Oxygen Evolution Reaction. *J. Phys. Chem. C* **2019**, *123*, 8304−8311.

(29) Giannozzi, P.; Baroni, S.; Bonini, N.; Calandra, M.; Car, R.; Cavazzoni, C.; Ceresoli, D.; Chiarotti, G. L.; Cococcioni, M.; Dabo, I.; et al. QUANTUM ESPRESSO: a modular and open-source software project for quantum simulations of materials. *J. Condens. Matter Phys.* **2009**, *21*, 395502.

(30) Giannozzi, P.; Andreussi, O.; Brumme, T.; Bunau, O.; Buongiorno Nardelli, M.; Calandra, M.; Car, R.; Cavazzoni, C.; Ceresoli, D.; Cococcioni, M.; et al. Advanced capabilities for materials modelling with Quantum ESPRESSO. *J. Phys.: Condens. Matter* **2017**, *29*, 465901.

(31) Hamann, D. R. Optimized norm-conserving Vanderbilt pseudopotentials. *Phys. Rev. B: Condens. Matter Mater. Phys.* **2013**, *88*, 085117.

(32) Schlipf, M.; Gygi, F. Optimization algorithm for the generation of ONCV pseudopotentials. *Comput. Phys. Commun.* **2015**, *196*, 36−44.

(33) Perdew, J. P.; Burke, K.; Ernzerhof, M. Generalized Gradient Approximation Made Simple. *Phys. Rev. Lett.* **1996**, *77*, 3865−3868.

(34) Cococcioni, M.; de Gironcoli, S. Linear response approach to the calculation of the effective interaction parameters in the LDA + U method. *Phys. Rev. B: Condens. Matter Mater. Phys.* **2005**, *71*, 035105.

(35) Monkhorst, H. J.; Pack, J. D. Special points for Brillouin-zone integrations. *Phys. Rev. B: Solid State* **1976**, *13*, 5188−5192.

(36) Grimme, S. Semiempirical GGA-type density functional constructed with a long-range dispersion correction. *J. Comput. Chem.* **2006**, *27*, 1787−1799.

(37) Löwdin, P. O. On the Non-Orthogonality Problem Connected with the Use of Atomic Wave Functions in the Theory of Molecules and Crystals. *J. Chem. Phys.* **1950**, *18*, 365−375.

(38) Henkelman, G.; Arnaldsson, A.; Jónsson, H. A fast and robust algorithm for Bader decomposition of charge density. *Comput. Mater. Sci.* **2006**, *36*, 354−360.

(39) Andreussi, O.; Dabo, I.; Marzari, N. Revised self-consistent continuum solvation in electronic-structure calculations. *J. Chem. Phys.* **2012**, *136*, 064102.

(40) Stull, D.; Prophet, H. *JANAF Thermochemical Tables*, 2nd ed.; U.S. National Bureau of Standards: Washington, DC, 1971.

(41) Nørskov, J. K.; Rossmeisl, J.; Logadottir, A.; Lindqvist, L.; Kitchin, J. R.; Bligaard, T.; Jónsson, H. Origin of the Overpotential for Oxygen Reduction at a Fuel-Cell Cathode. *J. Phys. Chem. B* **2004**, *108*, 17886−17892.

(42) Reuter, K.; Scheffler, M. Composition, structure, and stability of RuO₂(110) as a function of oxygen pressure. *Phys. Rev. B: Condens. Matter Mater. Phys.* **2001**, *65*, 035406.

(43) Campbell, C. T.; Sellers, J. R. V. The Entropies of Adsorbed Molecules. *J. Am. Chem. Soc.* **2012**, *134*, 18109−18115.

(44) Tersoff, J.; Hamann, D. R. Theory of the scanning tunneling microscope. *Phys. Rev. B: Condens. Matter Mater. Phys.* **1985**, *31*, 805−813.

(45) Doudin, N.; Yuk, S. F.; Marcinkowski, M. D.; Nguyen, M.-T.; Liu, J.-C.; Wang, Y.; Novotny, Z.; Kay, B. D.; Li, J.; Glezakou, V.-A.; et al. Understanding Heterolytic H2 Cleavage and Water-Assisted Hydrogen Spillover on Fe3O4(001)-Supported Single Palladium Atoms. *ACS Catal.* **2019**, *9*, 7876−7887.

(46) Kendelewicz, T.; Kaya, S.; Newberg, J. T.; Bluhm, H.; Mulakaluri, N.; Moritz, W.; Scheffler, M.; Nilsson, A.; Pentcheva, R.; Brown, G. E. X-ray Photoemission and Density Functional Theory Study of the Interaction of Water Vapor with the Fe3O4(001) Surface at Near-Ambient Conditions. *J. Phys. Chem. C* **2013**, *117*, 2719−2733.

(47) Liao, P.; Keith, J. A.; Carter, E. A. Water Oxidation on Pure and Doped Hematite (0001) Surfaces: Prediction of Co and Ni as Effective Dopants for Electrocatalysis. *J. Am. Chem. Soc.* **2012**, *134*, 13296−13309.

(48) Liang, Q.; Brocks, G.; Bieberle-Hütter, A. Oxygen evolution reaction (OER) mechanism under alkaline and acidic conditions. *J. Phys. Energy* **2021**, *3*, 026001.

(49) Man, I. C.; Su, H. Y.; Calle-Vallejo, F.; Hansen, H. A.; Martínez, J. I.; Inoglu, N. G.; Kitchin, J.; Jaramillo, T. F.; Nørskov, J. K.; Rossmeisl, J. Universality in Oxygen Evolution Electrocatalysis on Oxide Surfaces. *ChemCatChem* **2011**, *3*, 1159−1165.

(50) Shinagawa, T.; Garcia-Esparza, A. T.; Takanabe, K. Insight on Tafel slopes from a microkinetic analysis of aqueous electrocatalysis for energy conversion. *Sci. Rep.* **2015**, *5*, 13801.

(51) Peng, Y.; Hajiyani, H.; Pentcheva, R. Influence of Fe and Ni Doping on the OER Performance at the Co3O4(001) Surface: Insights from DFT+U Calculations. *ACS Catal.* **2021**, *11*, 5601−5613.

(52) Govind Rajan, A.; Martirez, J. M. P.; Carter, E. A. Facet-Independent Oxygen Evolution Activity of Pure -NiOOH: Different Chemistries Leading to Similar Overpotentials. *J. Am. Chem. Soc.* **2020**, *142*, 3600−3612.